J Therm Spray Tech (2019) 28:1945–1958
https://doi.org/10.1007/s11666-019-00941-6

PEER REVIEWED

Computational Research on Factors Affecting Particle Velocity in a Vacuum Kinetic Spray Process

Hyungkwon Park[1] · **Hansol Kwon**[2] · **Yeonju Kim**[2] · **Changhee Lee**[2]

Submitted: 10 June 2019 / in revised form: 16 October 2019 / Published online: 12 November 2019

Abstract In vacuum kinetic spraying (VKS) systems, also called aerosol deposition, the particle velocity is crucial because kinetic energy determines successful deposition. However, various factors simultaneously affect particle velocity, which complicates prediction. To address this issue, the factors affecting particle velocity in the VKS process were investigated via computational simulation. The factors were analyzed in terms of particle variables (i.e., particle material, size, and shape factor) and process variables (i.e., process gases and the pressure difference between the two chambers). Consequently, how and to what extent each factor influenced particle average and impact velocity are discussed.

Keywords aerosol deposition (AD) · computational fluid dynamics (CFD) · particle flight · particle velocity · vacuum kinetic spraying (VKS) process

Introduction

The vacuum kinetic spraying (VKS) process, also known as aerosol deposition (AD), is a technique used primarily for fabrication of dense ceramic films. The process has many advantages, including room temperature processing, facile coating-layer thickness control, and low cost (Ref 1, 2). For application development, VKS has been applied to produce films of various ceramic materials (Ref 2). Moreover, it has been recently reported from several researchers that the VKS process can be expanded to use with a variety of materials, including metals, polymers, and composites (Ref 3–7).

In the VKS process, relatively fine submicron particles are typically used. Initially, a powder of the particles is put into an aerosol chamber, where it is aerosolized by chamber vibration. Meanwhile, the other chamber in the system, called the deposition chamber, is sufficiently evacuated. Subsequently, the aerosolized particles are carried by a process gas into the deposition chamber through a pipe that connects the two chambers. The particles are drastically accelerated up to the high velocity of several hundred meters per second, impact the target, and are deposited within very a short time. The principle of the deposition process is simple, but the detailed deposition mechanism is still unclear because various complicated phenomena simultaneously occur, making it difficult to decouple the various contributions (Ref 8–15).

From what is known about the acceleration and deposition processes, several clues can be hypothesized. First, the whole process proceeds at room temperature; thus, successful particle deposition must completely depend on the kinetic energy of the inflight particle, as there are no other energy sources. In this respect, since the kinetic energy is highly related to particle velocity, the particle

---

Electronic supplementary material The online version of this article (https://doi.org/10.1007/s11666-019-00941-6) contains supplementary material, which is available to authorized users.

✉ Changhee Lee
chlee@hanyang.ac.kr

[1] Research & Development (R&D) Center, Hyundai Steel Company, Dangjin-Si, Chungnam 31719, South Korea

[2] Kinetic Spray Coating Laboratory (NRL), Division of Materials Science and Engineering, Hanyang University, Seongdong-Gu, Seoul 04763, South Korea

velocity must be a crucial factor in determining the bonding between deformed particles or fragments. Consequently, estimation of particle velocity is the most basic step to understanding the deposition process.

In addition, it can be conjectured that the factors affecting particle velocity can be categorized as either particle or process variables. For a given material, the particle mass, size, and shape are included in particle variables (Ref 16–19). These factors affect the drag force through the interaction between the gas stream and the particles, flowability in the gas, and the inertial movement of the particles (Ref 20–24). The process variables include the pressure difference between two chambers, nozzle geometry, kinds of gases used, and gas flow rates. In a VKS system, it is thought that the pressure difference between the two chambers is the main factor that determines the gas and particle velocities. With a high pressure difference between the chambers, a high velocity can be realized, even when using relatively low gas pressure. In addition, the gas flow rate is primarily used to fine tune the velocity because it is the easiest factor to control. Kinds of nozzles and gases are the variables that significantly affect the velocity, but both of these parameters are usually predetermined and unchangeable during any single experiment (Ref 24–26). Each of the factors acts to influence particle velocity in complex ways. Hence, predetermining the particle velocity for a VKS process is challenging.

In our previous research, a reliable prototype model was derived based on the experimental results (Ref 27); in addition, inflight particle behavior was researched using three kinds of Al_2O_3 powders with different sizes. Based on fundamental results, the various factors affecting particle velocity were investigated computationally in this study. First, the effects of particle parameters on particle velocity were investigated in "Particle Material Effect" and "Particle Shape Effect" sections using various particle materials with different sizes and shapes were applied. Twelve kinds of materials were investigated, including ceramics, metals, glasses, and polymers (these materials have either already been used in previous investigations or are anticipated to be applied in the near future). The shape effect was examined using a shape factor, which is very meaningful especially when the process uses irregularly shaped or pretreated particles. Second, the influence of process variables on the particle velocity was analyzed in "Process Gas Effect" and "Pressure Difference Effect Between the Two Chambers" sections; the behavior difference between helium (He) and nitrogen (N_2) gases and impact of the pressure difference between two chambers were studied. He gas is usually used for wide velocity control, while N_2 gas is often used due to relatively low cost. These results are crucial to enabling the prediction of VKS particle velocity and to determining the kinetic energy of particles.

Computational Method

Governing Equations

In this study, the commercial computer software ANSYS FLUENT v. 13.0 was used to analyze various particle behaviors in a VKS system. In the simulation, the gas is considered an ideal gas that undergoes steady-state turbulent compressible flow (Ref 28). The Navier–Stokes equation was fully solved by the software (Ref 29). The gas flow motion was governed by mass (continuity), momentum, and energy conservation equations (Ref 29):

$$\frac{\partial \rho_F}{\partial t} + \nabla \cdot (\rho_F \vec{v}_F) = S_m, \qquad \text{(Eq 1)}$$

$$\frac{\partial}{\partial t}(\rho_F \vec{v}_F) + \nabla \cdot (\rho_F \vec{v}_F \vec{v}_F) = -\nabla p + \nabla \cdot (\bar{\tau}) + p\vec{g} + \vec{F}_e, \qquad \text{(Eq 2)}$$

$$\frac{\partial \rho_F E}{\partial t} + \nabla \cdot (\vec{v}_F(\rho_F E + \rho_F)) = -\nabla \cdot \left(\sum_j h_j \cdot J_j\right) + S_h, \qquad \text{(Eq 3)}$$

where ρ_F is gas density (fluid), t is time, $\vec{v_F}$ is the velocity vector of the fluid, S_m is the mass added to the continuous phase from the dispersed second phase, p is the pressure, $\bar{\tau}$ is stress tensor, $\vec{g}$ is gravitational acceleration, $\vec{F}$ is an external body force vector, E is the total energy, h is the species enthalpy, J is the mass flux, and S_h is the volumetric heat source. All equations are referred and explained in detail in the ANSYS FLUENT (fluent) theory guide (Ref 29). In addition, the Reynolds-averaged Navier–Stokes (RANS) equation was applied for the statistical turbulent model, and a realizable κ–ε model was chosen. A density-based solver was applied to solve high-speed compressible gas flow. For simulation accuracy, second-order-accurate computations are used. A more detailed explanation can be found in our previous paper (Ref 27).

Modeling Design and Boundary Conditions

Figure 1(a) shows a schematic of the VKS system. Aerosolized particles in an aerosol chamber flow into the deposition chamber that is vacuumized using rotary and booster pumps. The gas pressure was fixed to 0.6 MPa by a gas pressure regulator, and the gas flow rate was usually adjusted within a range of 1–20 L/min. In addition, deposition trials generally began when the pressure of the deposition chamber was approximately 8 Pa. A slit-type convergent-barrel nozzle with an orifice of $5.0 \times 0.4\ \text{mm}^2$ was used, and the working distance between the nozzle exit and the substrate was set to 10 mm (Ref 14, 27). Figure 1(b) shows the three-dimensional simulation modeling

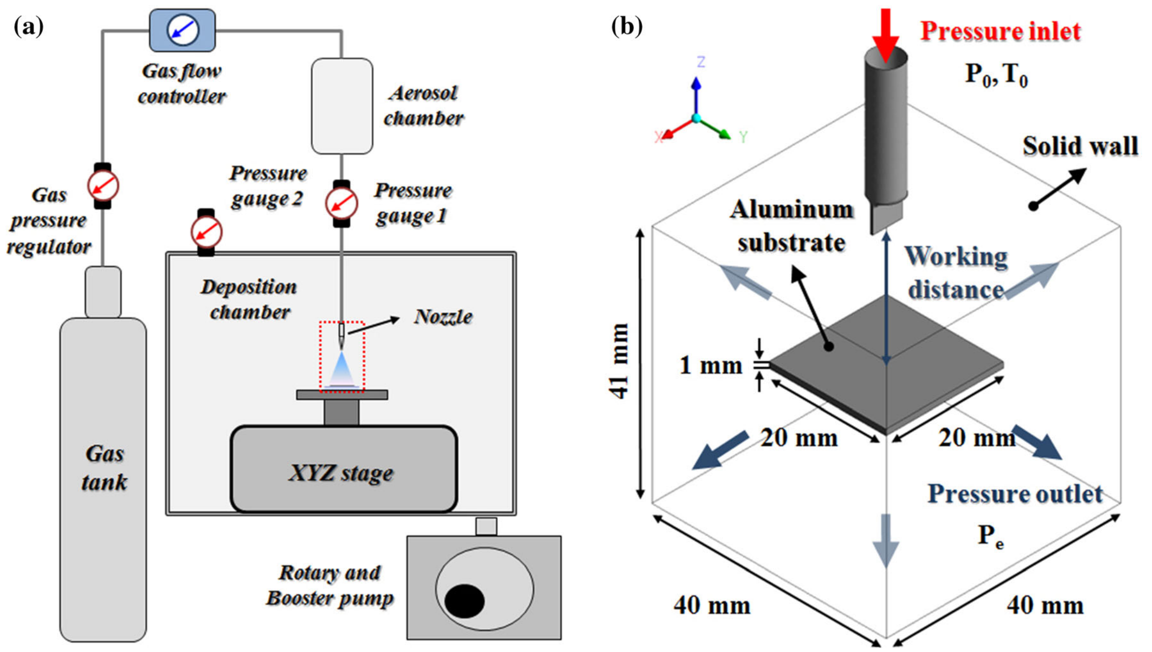

Fig. 1 (a) Schematic of a vacuum kinetic spraying system and (b) fluent simulation modeling design

design, and the simulation was applied in the vicinity between the nozzle entrance and the substrate, as marked by the red dashed box in Fig. 1(a). The behaviors of gas and particles were simulated in this region (Ref 27). The vacuum box had dimensions of 40 × 40 × 41 mm^3, and the Al substrate had dimensions of 20 × 20 × 1 mm^3 and was placed in the center of the vacuum box with a 10 mm distance from the nozzle exit. The mesh size was set from 1.0×10^{-6} to 3.0×10^{-3} m, the size of which was sufficient for simulation accuracy (Ref 27, 28).

The pressure inlet condition, P_0, was applied at the plane of the nozzle entrance, and the pressure could be directly measured at pressure gauge 1. The pressure values were measured from 11,332 to 30,664 Pa in the case of He gas and from 18,665 to 50,663 Pa in the case of N_2 gas, as the gas flow rate increased from 6 to 18 L/min (although a gas flow rate of 2 L/min was calculated using the extrapolation method in previous research (Ref 27), that case was excluded in this research). The nozzle entrance temperature, T_0, was set to room temperature, 298 K. The condition of pressure outlet, P_e, was applied to five walls of the vacuum box, as indicated by blue arrows in Fig. 1(b). Because it was impossible to directly measure the pressure outlet (pressure gauge 2 was placed away from the simulation region, and the pressure at this location was influenced by the gas stream), the value was set to 4000 Pa based on the experimental results in our previous study (Ref 27). The exception to this is in "Pressure Difference Effect Between the Two Chambers" section, in which the pressure outlet was varied from 1000 to 10,000 Pa to investigate the pressure difference effect. A no-slip boundary condition was applied to the nozzle wall, and the working distance from nozzle exit to substrate was set to 10 mm (except in "Process Gas Effect" section, in which this value was varied up to 15 mm) (Ref 14, 27). The boundary conditions are listed in Table 1.

Discrete Phase Model

To analyze the particle trajectory in a flow field, the Lagrangian phase discrete model (DPM) was applied. Dispersed phase was solved by tracking numerous particles through the calculated flow field, while fluid phase was considered as a continuum solved by the Navier–Stokes equations. In the simulations, the particles were diluted sufficiently in the fluid; thus, it was assumed that the interaction among particles could be neglected, and the influence of particles on the gas state, including velocity and temperature, was negligible (Ref 21, 27, 28). Only the drag force from gas-dynamics was considered to have an effect on particle velocity. The discrete phase trajectory

Table 1 Boundary conditions for He and N_2 gases

Process gas	He	N_2
Pressure inlet, Pa	11,332–30,664	18,665–50,663
Pressure outlet, Pa	1000–8000	4000
Wall condition	No-slip boundary	
Working distance, mm	10, 15	

was predicted based on force balance, which equates the particle inertia with the forces acting on the particle, expressed as (Ref 29):

$$\frac{\mathrm{d}\vec{v}_P}{\mathrm{d}t} = F_D(\vec{v}_F - \vec{v}_P) + \frac{\vec{g}(\rho_P - \rho_F)}{\rho_P} + \vec{F}_a \qquad \text{(Eq 4)}$$

where $\vec{v}_P$ is the particle velocity, ρ_P is the particle density, and $\vec{F}_a$ is an additional acceleration (force/unit particle mass) term. In addition, $F_D(\vec{v}_F - \vec{v}_P)$ is the drag force per unit particle mass, and the term F_D is defined as (Ref 29):

$$F_D = \frac{18\mu}{\rho_P d_P^2} \frac{C_D \mathrm{Re}}{24} \qquad \text{(Eq 5)}$$

where μ is the molecular viscosity of the fluid, d_p is the particle diameter, and C_D is the drag coefficient. In addition, R_e is the relative Reynolds number indicating the ratio of inertial forces to viscous force and is expressed as (Ref 29):

$$R_e \equiv \frac{\rho_F d_P |\vec{v}_P - \vec{v}_F|}{\mu}. \qquad \text{(Eq 6)}$$

From these equations, it is evident that various factors including gas velocity, particle diameter, and particle and gas densities affect the particle velocity in a flow field.

In addition, the particles were injected vertically and uniformly into the nozzle entrance and accelerated through the nozzle. After nozzle exit, some of the particles impacted the substrate, while others continued along the gas flow to escape the wall of a vacuum box. When the particles reached the substrate, they were eliminated from the simulation, assuming ‘impact.’ The others were regarded as ‘escaped.’ Accordingly, the impact probability was readily calculated as

$$\text{Impact probability} = \frac{\text{Impact particles}}{\text{Total particles}} \times 100\% \qquad \text{(Eq 7)}$$

Here, the total particles are the sum of impacted and escaped particles. The impact probability is an important parameter because only the particles that impact the target can participate in deposition.

Furthermore, the particle shape effect was investigated. For this study, the particle shape factor, ϕ, is defined as

$$\Phi = \frac{A_s}{A_p} \qquad \text{(Eq 8)}$$

where A_s is the surface area of a sphere having the same volume as the particle, and A_p is the actual surface area of the particle; that is, ϕ indicates a sphericity of the particle (Ref 30). This factor ranges from 0 to 1, where 1 is completely spherical while the particle becomes non-spherical, such as cylindrical or ellipsoidal particle, as the value approaches 0. The Reynolds number, $R_{e,\mathrm{sph}}$, is computed with the diameter of a sphere of the same volume (Ref 29).

In this study, 20 kinds of materials were applied to the discrete phase including ceramics, amorphous materials, metals, and polymers, as listed in Table 2. Those materials have been used as feedstock materials or have potential applicability for a film. Al_2O_3 was chosen as a representative material for comparison because the model was based on Al_2O_3 deposition results. In addition, density-dependent particle behavior was evaluated based on the behaviors of polyimide (PI, lightest), Y_2O_3 (intermediate), and Ag (heaviest) as representative materials.

Results and Discussion

Particle Material Effect

Figure 2 shows the particle average and impact velocity of various materials with different particle sizes and He gas flow rates (additionally, the specific values of the other material velocities with different sizes and gas flow rates are listed in Supplementary Table 1). In Fig. 2(a), the average velocity of Al_2O_3 particles decreased as the size increased from 0.5 to 2.0 μm. On the other hand, the 0.5 μm particle showed the lowest impact velocity, although it became higher with increased gas flow rate. Meanwhile, the other sizes exhibited similar impact velocities, but the slope decreased with increased particle size. The average velocity of PI behaved slightly differently from the other materials. Although the results of the 1.0–2.0 μm particles were similar to those of other particles, the average velocity of the 0.5 μm particle rose steeply and linearly with gas flow rates. It is probable that the small PI particle responded quickly to changes in gas flow due to its light density. It is notable that the impact velocity of 0.5 μm PI was very low (4–25 m/s); that is, the impact velocity, which is defined to be along the *z*-axis, was almost zero, although the *x*- and *y*-velocities were probably nonzero. This means that the smallest sized PI particle studied had difficulty impacting the substrate with sufficiently high velocity for deposition. In addition, the larger was the particle size, the higher was the impact velocity. This trend is opposite that of the Al_2O_3 particles, except for the 0.5 μm case. It was concluded that the velocity of PI particles was significantly affected by the positive and negative drag forces of the gas stream, including gas deflecting from the substrate (Ref 27). The trend of Y_2O_3 particle velocity was similar to that of Al_2O_3 due to similar density values, but the velocities of Y_2O_3 particles were slightly lower than those of comparable Al_2O_3 particles because the density of Y_2O_3 is a bit higher than that of Al_2O_3. It is worth noting that, for both Al_2O_3 and Y_2O_3 particles, the impact velocities of particles having smaller than 1.0 μm (0.5 and 1.0 μm) linearly risen

Table 2 Discrete phase constants of various materials

	Materials	Density, g/cm^3	Cp, J/g-k	Thermal conductivity, W/m k
Ceramic	Al_2O_3	3.960	0.753	30
	TiO_2	3.890	0.714	13
	TiN	5.220	0.752	19
	AlN	3.260	0.74	285
	B_4C	2.520	0.950	50
	SiC	3.215	0.670	122
	PZT	7.800	0.430	1.2
	ZnO	5.606	0.495	30
	Y_2O_3	5.010	0.460	14
	YSZ	6.050	0.400	2
Amorphous	BMG	7.650	0.550	10
	Glass	2.230	0.830	1.12
Metal	Ti	4.850	0.544	7.44
	Steel	8.030	0.503	16.27
	Cu	8.978	0.381	387.6
	Zn	7.100	0.390	111.2
	Ag	10.491	0.234	419
Polymer	PC	1.210	1.200	0.20
	PI	0.943	1.045	0.25
	PMMA	1.170	0.385	0.19

while those of particles having larger than 1.5 μm (1.5 and 2.0 μm) parabolically increased and seemed to converge to a specific limit based on gas flow rates. In terms of mass, the velocity of light particles increased more linearly as gas flow rate increased. The heaviest material, Ag, generally showed the lowest average and impact velocities. Meanwhile, it is notable that the smallest Ag particle of 0.5 μm showed a high impact velocity compared to the other materials having same size, and the impact velocity increased linearly with gas flow rate, although other Ag sizes did not. It is thought that Ag has very high density, so that it is less affected by negative drag force despite its small size. From this perspective, it is understandable that 0.5 μm Ag had a high average velocity, and that the velocity gap between 0.5 and 1.0 μm was significantly high.

The *z*-axis velocities change along the path length of each particle material and He gas at 18 L/min gas flow rate are shown in Fig. 3(a). The gas velocity was abruptly accelerated as it passed through the convergent part of the nozzle and then gradually increased until it left the nozzle. The velocity was maximized at the nozzle exit around 1100 m/s; in the vicinity, the Mach number was greater than 1. However, after this region, the velocity suddenly dropped to around 800 m/s and continued to decrease slightly until about 5 mm from the nozzle exit. Thereafter, the gas velocity decreased dramatically due to gas deflecting from the substrate. This gas acceleration and deceleration provide positive and negative drag force, respectively, to particles. However, because the particles have specific densities that are higher than that of the gas, they can resist the negative force of the gas with their inertia. Therefore, the particle velocity does not drop to zero, and the particle can impact the substrate with significantly high velocity of several hundred meters per second. In addition, the materials with higher density maintain their velocities better through deflecting gas flow and thus can impact with high velocity. However, high-density materials have an advantage in terms of resisting negative drag force but also have a disadvantage from the perspective of acceleration; that is, high-density materials experience less acceleration due to their higher weight. On the other hand, light materials have difficultly impacting the target and easily flow with the gas stream until exiting the vacuum box. Thus, the impact probability of light materials is low. Figure 3(b) presents the impact probability of PI with different particle sizes and gas flow rates. Over 70% of the 0.5 μm PI particles passed through the simulation region without substrate impact. Therefore, with light materials, small particles are not suitable for deposition; use of particles larger than 1.0 μm is more appropriate. As a result, particle average and impact velocity are significantly influenced by particle mass, which is determined by material density and particle size. Therefore, to optimize impact velocity, both material density and particle size must be considered.

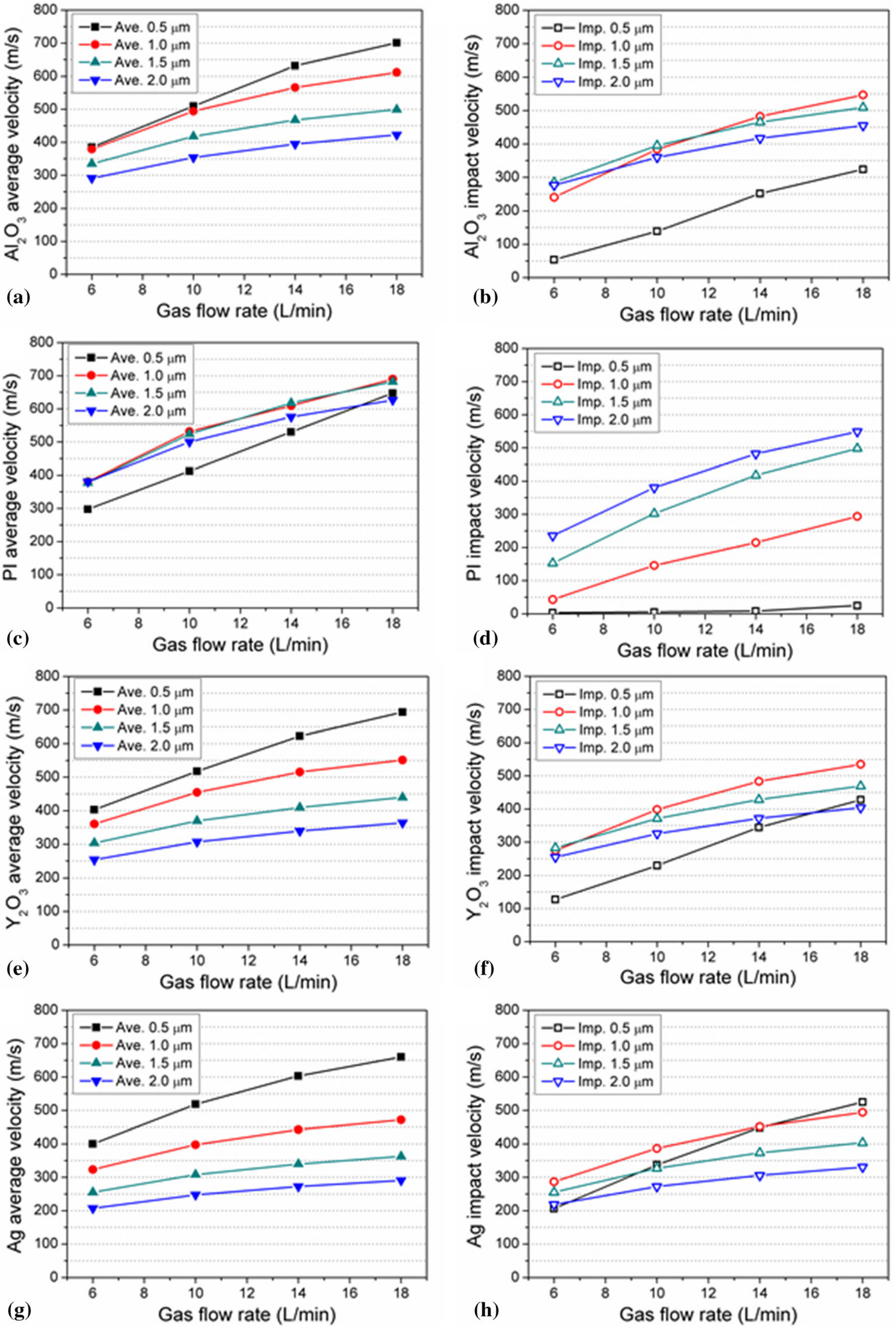

Fig. 2 Particle average and impact velocity of (a-b) Al_2O_3, (c-d) PI, (e-f) Y_2O_3, and (g-h) Ag particles with different sizes and He gas flow rates

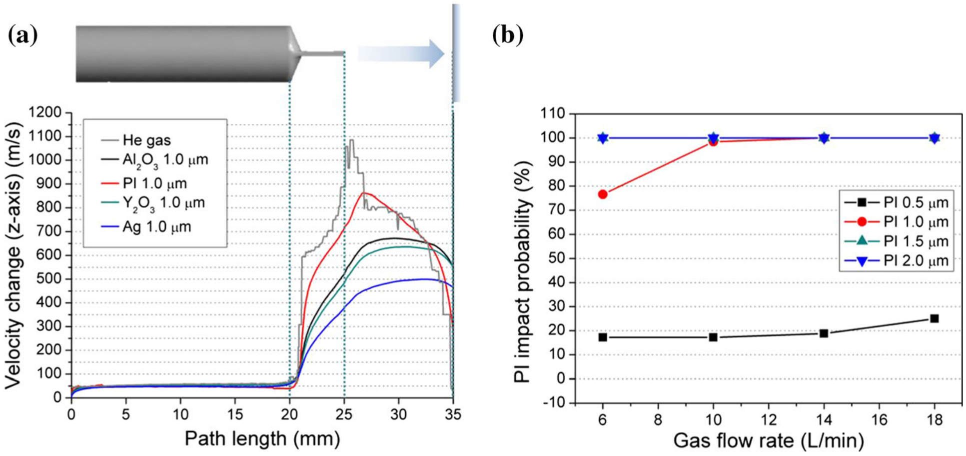

Fig. 3 (a) The velocity change of He gas and various particles along the *z*-axis at a He flow rate of 18 L/min, and (b) PI particle impact probability with different He gas flow rates

Particle Shape Effect

In VKS, pre-treatments like milling are frequently applied to increase deposition efficiency or decrease powder size (Ref 1, 31–33). During pre-treatment, particle shape change is inevitable. Therefore, it necessary to consider the velocity changes that may result from shape changes. Figure 4 shows the particle average and impact velocity of various materials with different particle shape factors ranging from 0.2 to 1.0 and different He gas flow rates. For this study, the particle diameter was fixed at 1.0 μm, but the surface area differed according to a shape factor. In Fig. 4(a), it is evident that the increase tendency of Al_2O_3 particle average velocity with gas flow rates was similar to that above; as shape factor decreased (1.0 → 0.2), the particle accelerated slightly. Impact velocities (Ref Fig. 4(b)) of the particles with shape factors from 0.4 to 1.0 were similar, but particles with a shape factor of 0.2 showed comparably low impact velocities. Although the 0.2-shape factor particles have the same mass as the other particles in this study, these flattened particles behave as if they are small; that is, it is inferred that the decreased impact velocity can attribute to sensitivity to deflecting gas for these particles. For PI, as gas flow rate increases, the average velocity increases linearly with shape factors of 0.2 and 0.4 and increases parabolically for shape factors of 0.6, 0.8, and 1.0, as shown in Fig. 4(c). In Fig. 4(d), despite low impact velocity, the impact velocity tendency with gas flow rate was similar to size effect in Fig. 2(d); the 0.2 shape factor particle was sensitive to negative drag force, similar to the 0.5 μm particle. In general, Y_2O_3 [Fig. 4(e) and (f)] showed a similar trend in average and impact velocities to Al_2O_3. In the case of Ag, the trend in average velocity was similar to Al_2O_3 but the impact velocity was less affected by a shape factor than Al_2O_3, as shown in Fig. 4(g) and (h). It is inferred that Ag particle is less decelerated because of the high density.

Figure 5(a) and (b) indicates the *z*-axis velocity changes of 1.0 μm Al_2O_3 and 2.0 μm Ag particles, respectively, along the path length with different shape factors (SF) at a gas flow rate of 10 L/min. It can be observed that the 0.2-shape factor Al_2O_3 particle was more highly accelerated than the others as it passes the nozzle and decelerates in the vicinity of the substrate; in other words, the particle with a lower shape factor is more sensitive to gas flow. In contrast, as the shape becomes more spherical, the particle response decreases. Considering that ball-milled brittle particles occasionally have flake-like shapes, it can be inferred that the sensitivity to gas flow will increase with ball-milling. On the other hand, it is worth noting that the 2.0 μm Ag particle with a shape factor of 0.2 showed a higher impact velocity than the others in Fig. 5(b). From this, it is concluded that impact velocity inversely increased as a shape factor decreased in material of high-density and large size. From this perspective, it is understandable that ball-milled bulk metallic glass (BMG) particles (7.65 g/cm^3) are able to be successfully deposited despite the flake-like shapes resulting from severe ball-milling in our previous research, as the particle sizes were large (Ref 32). Additionally, the impact probability of PI with different shape factors is shown in Fig. 5(c). As a shape factor decreased, impact probability decreased, even though particle size was constant. Consequently, particle velocity, especially impact value, changes depending on particle shape. Thus, the shape factor should be considered as a factor controlling particle impact velocity.

Process Gas Effect

Figure 6 represents the velocity change of He and N_2 gas with 1 μm Al_2O_3 particles along the path length at 10 L/min. The figure confirms that a 1 μm particle has a considerably higher velocity in He gas than in N_2 gas, even when the gas flow rates are identical. Both gases were

Fig. 4 Particle average and impact velocity of 1-μm (a-b) Al_2O_3, (c-d) PI, (e-f) Y_2O_3, and (g-h) Ag particles with different shape factors and He gas flow rates

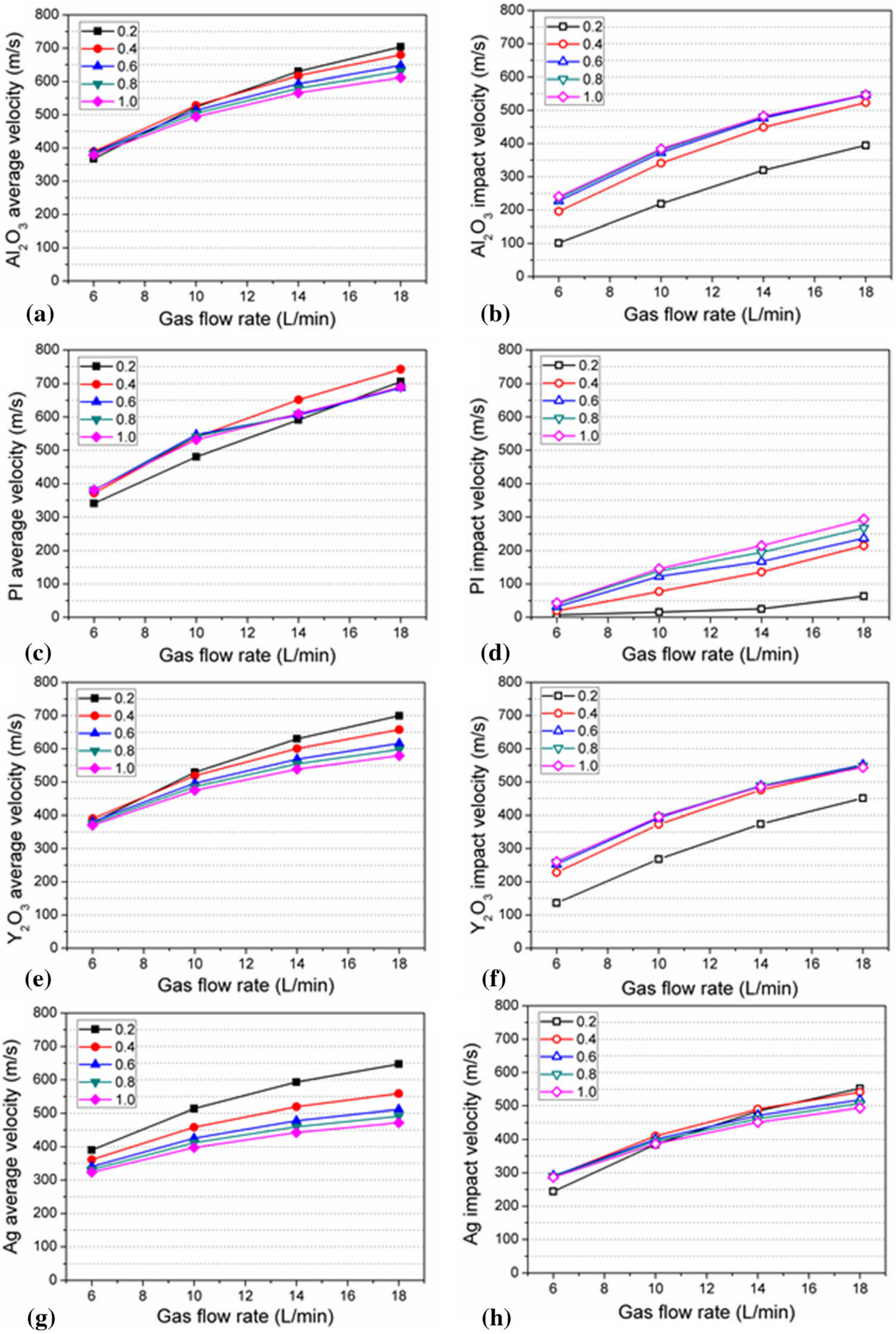

accelerated as they passed through the nozzle and achieved maximum velocity just after exiting the nozzle. However, the degree of acceleration was significantly different although the pressure outlet was set to a higher value for N_2 (29,331 Pa) than for He (17,332 Pa). This can probably be attributed to gas density; N_2 (1.2504 kg/m^3) has higher density than He (0.1786 kg/m^3). Accordingly, the degree of acceleration could vary greatly for a given particle.

Using N_2 gas, the particle average and impact velocities of various materials with different sizes are shown in Fig. 7. In Fig. 7(a), the average velocity of the 1 μm Al_2O_3 particles changed slightly from 240 to 318 m/s with gas flow rate. In particular, the particle size did not have a large effect on average velocity, which had a maximum value of 83 m/s at 14 L/min. However, impact velocity shows a different trend [Fig. 7(b)]. Even though the impact velocity

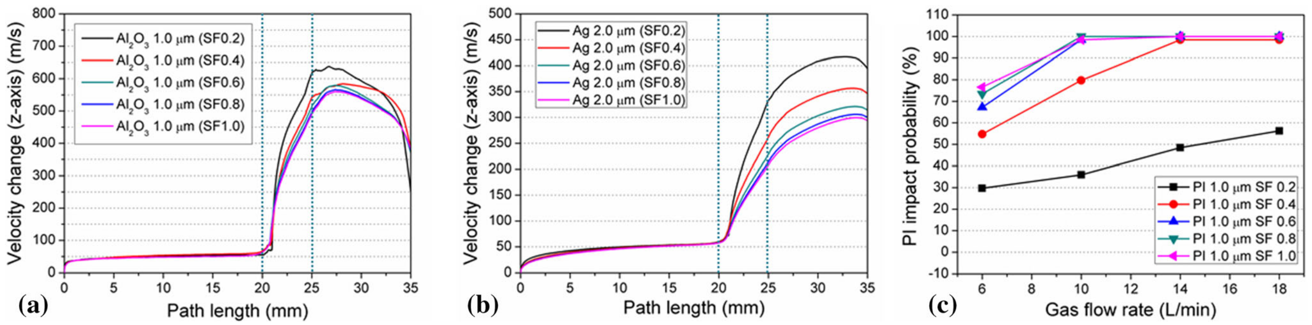

Fig. 5 Velocity change of (a) 1.0 μm Al_2O_3 and (b) 2.0 μm Ag particles, and (c) PI particle impact probability with different particle shape factors and He gas flow rates

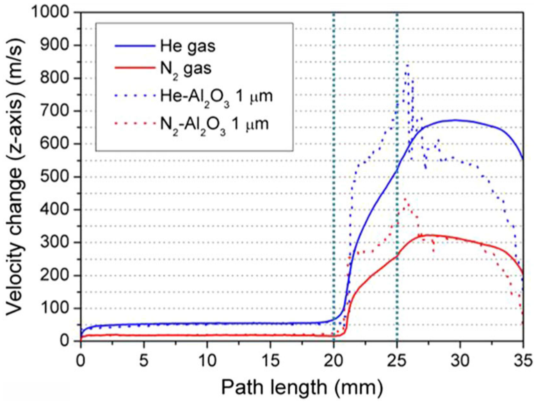

Fig. 6 Velocity change of He and N_2 gases with 1-μm Al_2O_3 particles at a gas flow rate of 10 L/min

of the 1 μm particle ranged from 144 to 235 m/s, and these velocities were similar for particles larger than 1.0 μm (1.0, 1.5, and 2.0 μm), the 0.5 μm particle had considerably lower impact velocity less than 100 m/s. It is thought that strong deflecting gas was generated by the high density of N_2 gas, and the degree of deceleration became larger than it would with He. Another interesting point is that the velocity decreases between 14 and 18 L/min. Because the pressure difference was larger, the velocities of gas and particle are likely to increase in general. This discrepancy will be discussed later.

The average velocity of 1 μm PI particles ranged from 242 to 304 mm/s, almost independent of particle size, as shown in Fig. 7(c). The velocity change as a function of size was within 10 m/s. On the other hand, impact velocity was relatively uniform across sizes [Fig. 7(d)]. From these results, it is concluded that, for light materials, the average velocity is similar for different sizes of particles, but the impact velocity is size-dependent. The average and impact velocities of Y_2O_3 were very similar to those of Al_2O_3, as shown in Fig. 7(e) and 7(f). This is reasonable because the two materials have similar densities and thus similar inflight behavior and reactivity to gas. Due to the slightly higher density of Y_2O_3, the average velocity gap was a bit larger with changes to particle size and the impact velocity of the 0.5 μm Y_2O_3 particles was slightly higher than that of the 0.5 μm Al_2O_3 particles. This trend became more obvious as material density increased, as shown for Ag in Fig. 7(g) and (h). As gas flow rate increased, the difference between average velocities at a specific particle size became progressively larger; the velocity difference at 14 L/min between 0.5 and 2.0 μm was 148 m/s. Moreover, the impact velocity of the 0.5 μm particles was significantly higher than that of the other sizes. Ag appears to have a density high enough to overcome the deceleration of deflecting gas, even with small particle size. Consequently, although the particle velocity was low using N_2 gas due to low gas velocity, the average and impact velocities changed according to particle size and material density. It is especially important to avoid the use of light materials or small sizes less than 1.0 μm to avoid low impact velocity that leads to deposition failure.

As mentioned above, the decrease in particle velocity despite the increase in gas flow rate from 14 to 18 L/min needs to be understood. Figure 8(a) and (b) represents the velocity change of 0.5 and 1.0 μm Al_2O_3 particles at 14 and 18 L/min at the working distances of 10 and 15 mm. In each figure, it is necessary to focus on the maximum particle velocity and the time to velocity decrease. At a 10 mm working distance, 0.5 and 1.0 μm particles reached particle velocities of 430 and 370 m/s, respectively, just after exiting the nozzle. At that time, the peak velocities were almost same, regardless of gas flow rates. However, the particle velocities began to drop a little faster at 18 L/min than at 14 L/min. Accordingly, this phenomenon caused the particles to impact the target with relatively lower velocity. It is thought that, as the gas flow rate passes a certain value, the force of deflecting gas increases, which results in greater particle deceleration. To weaken this influence, the working distance was set to farther, 15 mm [Fig. 8(b)]. These results confirm that increasing the working distance slightly increases the maximum velocity of the particles, and the impact velocity was higher at 18

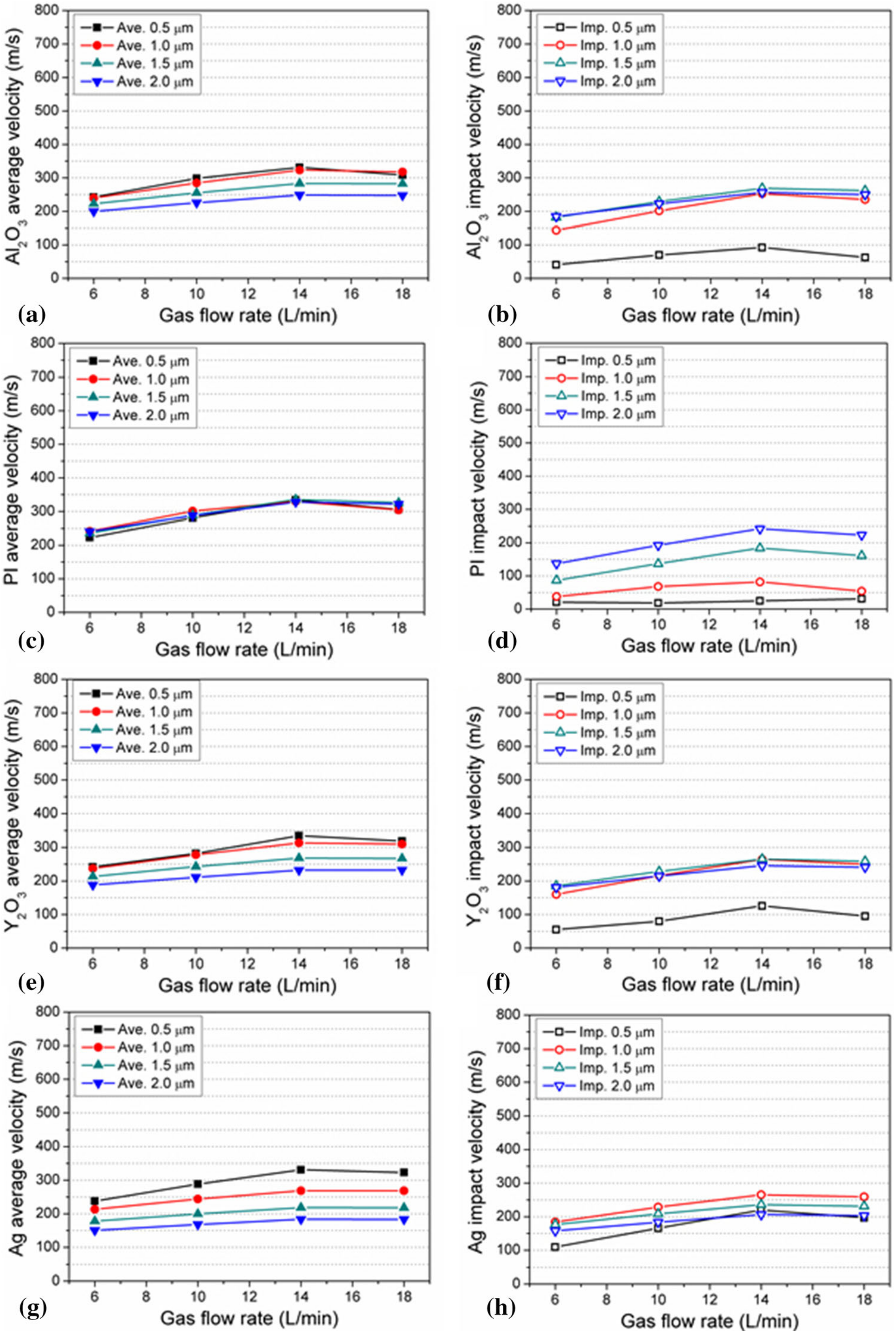

Fig. 7 Particle average and impact velocity of 1-μm (a-b) Al_2O_3, (c-d) PI, (e-f) Y_2O_3, and (g-h) Ag particles with different sizes and N_2 gas flow rates

L/min than at 14 L/min. Figure 9(a) shows N_2 gas velocity change along path length. It seems that the gas velocities of both 14 and 18 L/min have similar distribution from inlet to substrate, but the gas velocity of 18 L/min was not sufficiently accelerated (upper arrow). In addition, in the vicinity of the substrate, the N_2 gas velocity in 18 L/min greatly decreased compared with the 14 L/min (lower arrow) because of high back pressure. Figure 9(b) and (c) demonstrates the pressure intensity increases from 14 to 18 L/min in the vicinity of the substrate. Clearly, a higher pressure distribution formed at 18 L/min, which greatly decelerated the particle. In contrast, considering the lack of velocity decrease with increasing gas flow rate for He, it is inferred that this phenomenon is deeply related to gas density. As a result, when using high-density gases, the gas

Fig. 8 Velocity change of 0.5 and 1.0 μm Al_2O_3 particles at 14 and 18 L/min flow rates at working distances of (a) 10 and (b) 15 mm

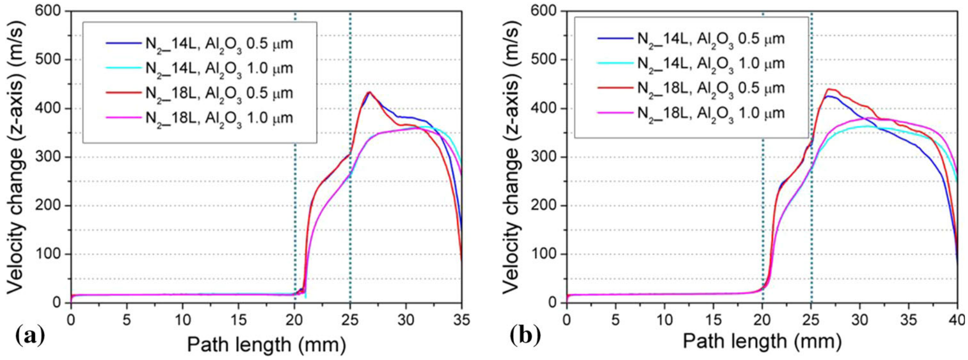

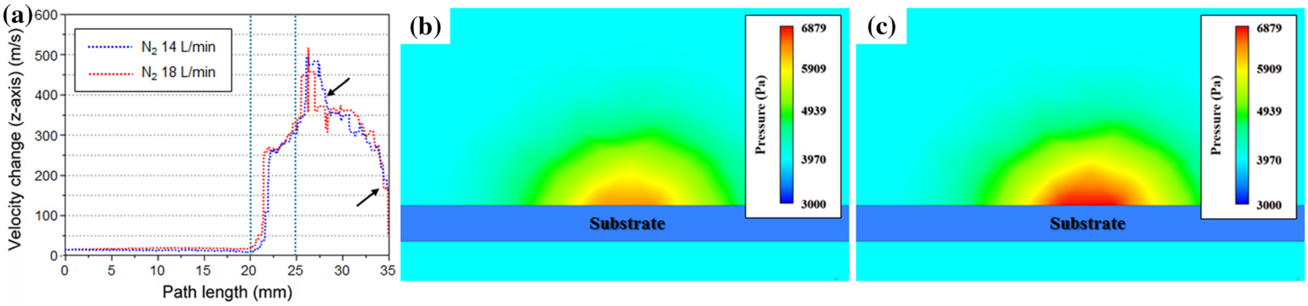

Fig. 9 (a) The velocity change of N_2 gas and pressure contour in the vicinity of the substrate at the gas flow rates of (b) 14 and (c) 18 L/min

flow rate must be utilized with an appropriate working distance to maximize the particle impact velocity.

Pressure Difference Effect Between the Two Chambers

Figure 10 shows the particle average and impact velocity change with various materials according to pressure outlet (denoted as PO) using He gas flow rate of 10 L/min. In this case, since the pressure inlet was set to 17,332 Pa (10 L/min), the change of pressure outlet reflects a variation of the pressure difference between two chambers. For all materials, as PO decreased, the particle velocity increased because the pressure difference increased. As shown in Fig. 10(a), the average and impact velocities of 1-μm Al_2O_3 particles were almost the same at about 680 m/s at PO = 1000 (denoted as PO1000), but the difference between two velocities increased as pressure difference diminished. In addition, the degree of velocity decrease had more of an effect on impact velocity than on average velocity. Consequently, the velocity of the Al_2O_3 particle decreased to 278 m/s on average and to 134 m/s at impact. The impact velocity dropped as much as 550 m/s with the decrease of pressure difference from PO1000 to PO10000. In conclusion, these results show that the pressure difference significantly affects both particle velocities.

Although the velocity trends of Y_2O_3 are similar to those of Al_2O_3, as confirmed in Fig. 10(c), it is worth noting that, in Fig. 10(b) and (d), the velocity trends of PI and Ag are considerably different. In the case of PI, the differential between the average and impact velocities was very large, from 247 (PO10000) to 379 m/s (PO1000). In contrast, Ag particles showed differentials of 58 (PO10000) and -63 (PO1000). At PO1000, the impact velocity was higher than the average velocity for Ag. In addition, the change of particle velocity was much higher for PI than for Ag. From these data, it is inferred that the velocity deviation of light particles is larger than that of heavy particles. This is because light material is more sensitive to the gas. Because heavy particles are less affected by acceleration and deceleration of gas, the impact velocity is occasionally higher than the average velocity in specific conditions. As a result, as pressure difference increases (PO decreases), the particle velocities significantly increase; moreover, as material density increases, the particle is less sensitive to pressure difference.

The velocity changes of gas and 1 μm Al_2O_3 particle are shown in Fig. 11(a) and (b), respectively. He gas was more accelerated as PO decreased; at the nozzle exit, gas temporarily went beyond 1000 m/s at PO1000 and PO2000; accordingly, a 1 μm particle impacted at 600–700 m/s. From this result, it is noted that pressure difference is an important factor affecting gas acceleration and subsequently particle velocity. Consequently, it is possible to increase the particle velocity by lowering the pressure of the deposition chamber. However, if the degree of vacuum

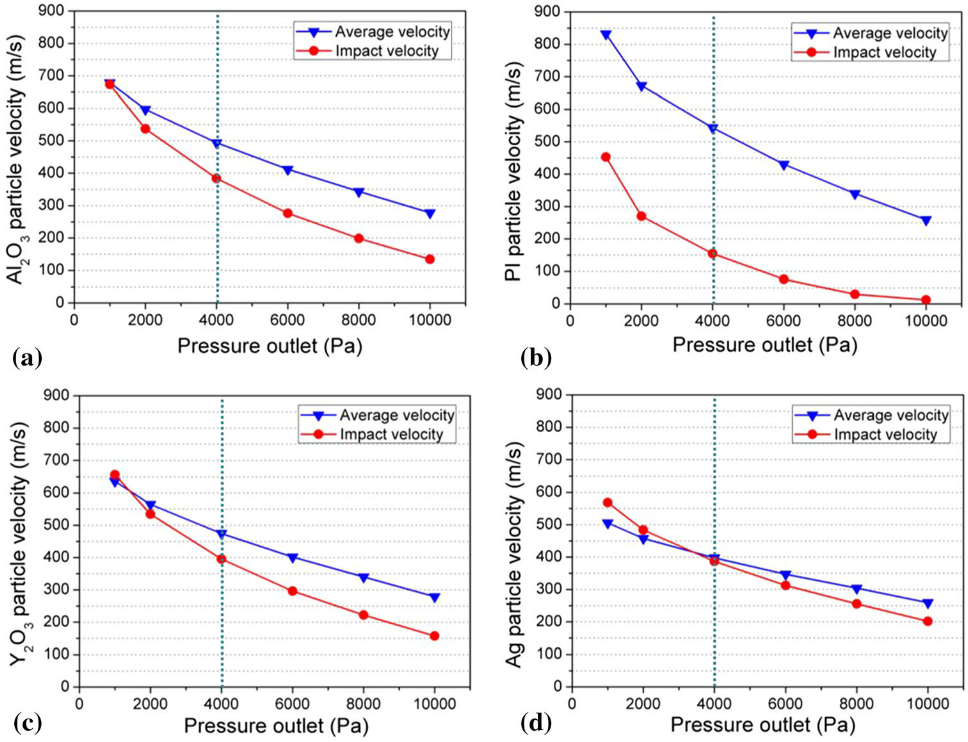

Fig. 10 Particle average and impact velocity of 1-μm (a) Al_2O_3, (b) PI, (c) Y_2O_3, and (d) Ag particles as a function of the pressure difference resulting from pressure outlet change at a He flow rate of 10 L/min

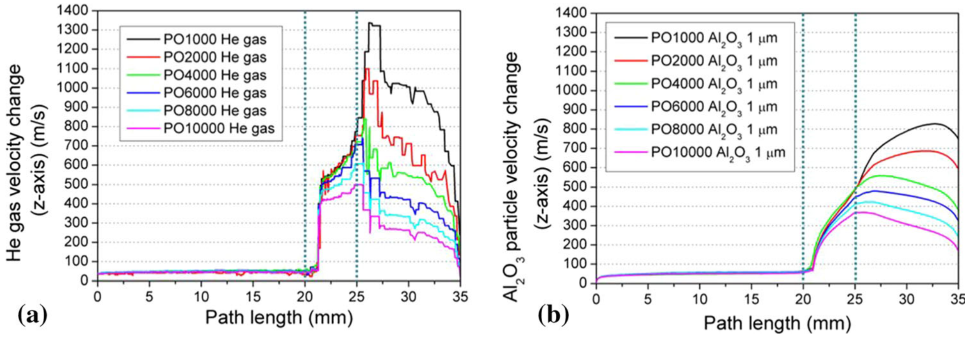

Fig. 11 (a) He gas and (b) 1-μm Al_2O_3 particle velocity change as a function of pressure outlet

increases, longer evacuation times will be needed, leading to a decrease in productivity. Therefore, it is important to optimize the velocity for deposition at a practical vacuum level.

Conclusion

In this research, the factors affecting particle velocity in the VKS process were investigated via computational simulation. Analysis was divided into particle parameters (material, particle size, and shape factor) and process parameters (process gases and pressure difference between aerosol and deposition chambers). The particle average and impact velocities were significantly influenced by particle mass, which is determined by material density and particle size. Particles with very low mass impacted with low velocity or did not impact the target at all due to the deceleration caused by deflecting gas; particles with excessively high mass were difficult to accelerate sufficiently. For a given particle volume, particles with a small shape factor (flat form) behaved as small-sized particles. Although flat-type particles could be unfavorable for high-speed impact of low-density materials or small particles, this shape effect could conversely become advantageous for high-density materials and large particle sizes. N_2 gas has higher density than He, and accordingly, particles were less accelerated. On the other hand, deceleration by deflecting gas was relatively strong when using N_2, which additionally hindered particle impact with high velocity. This effect is particularly noticeable for particles smaller than 1 μm or made of light materials. In addition, it is necessary to control the working distance to avoid excessive deceleration when using high-density gas. Pressure difference between the two chambers obviously has a significant effect on particle velocities. Therefore, lowering deposition chamber pressure is one possible way to maximize particle velocities. However, it is also important to optimize vacuum level considering process efficiency and productivity. Particle velocity is determined via the combination of various factors mentioned above; based on the findings, optimization of particle velocity to improve the deposition rate or efficiency in a VKS system can be achieved.

References

1. J. Akedo, Room Temperature Impact Consolidation (RTIC) of Fine Ceramic Powder by Aerosol Deposition Method and Applications to Microdevices, *J. Therm. Spray Technol.*, 2008, **17**(2), p 181-198
2. D. Hanft, J. Exner, M. Schubert, T. Stöcker, P. Fuierer, and R. Moos, An Overview of the Aerosol Deposition Method: Process Fundamentals and New Trends in Materials Applications, *J. Ceram. Sci. Technol.*, 2015, **6**(3), p 147-182
3. H.-J. Kim and S.-M. Nam, High Loading of Nanostructured Ceramics in Polymer Composite Thick Films by Aerosol Deposition, *Nanoscale Res. Lett.*, 2012, **7**(1), p 92
4. Y.-H. Kim, J.-W. Lee, H.-J. Kim, Y.-H. Yun, and S.-M. Nam, Silver Metallization for Microwave Device Using Aerosol Deposition, *Ceram. Int.*, 2012, **38**, p S201-S204
5. O.-Y. Kwon, H.-J. Na, H.-J. Kim, D.-W. Lee, and S.-M. Nam, Effects of Mechanical Properties of Polymer on Ceramic-Polymer Composite Thick Films Fabricated by Aerosol Deposition, *Nanoscale Res. Lett.*, 2012, **7**(1), p 261
6. J.H. Lee, H.-K. Kim, S.-H. Lee, K. Choi, and Y.-H. Lee, Effect of Zn Filler for Percolative $BaTiO_3$/Zn Composite Films Fabricated by Aerosol Deposition, *Ceram. Int.*, 2015, **41**(9), p 12153-12157
7. M.-Y. Cho, D.-W. Lee, W.-J. Kim, Y.-N. Kim, S.-M. Koo, D. Lee, K.-S. Moon, and J.-M. Oh, Fabrication of TiO_2/Cu Hybrid Composite Films with Near Zero TCR and High Adhesive Strength Via Aerosol Deposition, *Ceram. Int.*, 2018, **44**(15), p 18736-18742
8. D.W. Lee, H.J. Kim, Y.H. Kim, Y.H. Yun, and S.M. Nam, Growth Process of α-Al_2O_3 Ceramic Films on Metal Substrates Fabricated at Room Temperature by Aerosol Deposition, *J. Am. Ceram. Soc.*, 2011, **94**(9), p 3131-3138
9. F. Cao, H. Park, G. Bae, J. Heo, and C. Lee, Microstructure Evolution of Titanium Nitride Film During Vacuum Kinetic Spraying, *J. Am. Ceram. Soc.*, 2013, **96**(1), p 40-43
10. B. Daneshian and H. Assadi, Impact Behavior of Intrinsically Brittle Nanoparticles: A Molecular Dynamics Perspective, *J. Therm. Spray Technol.*, 2014, **23**(3), p 541-550
11. H. Park, J. Kim, and C. Lee, Dynamic Fragmentation Process and Fragment Microstructure Evolution of Alumina Particles in a Vacuum Kinetic Spraying System, *Scripta Mater.*, 2015, **108**, p 72-75
12. H. Park, J. Kwon, I. Lee, and C. Lee, Shock-Induced Plasticity and Fragmentation Phenomena During Alumina Deposition in the Vacuum Kinetic Spraying Process, *Scripta Mater.*, 2015, **100**, p 44-47
13. Y. Liu, Y. Wang, X. Suo, Y. Gong, C.-J. Li, and H. Li, Impact-Induced Bonding and Boundary Amorphization of TiN Ceramic Particles During Room Temperature Vacuum Cold Spray Deposition, *Ceram. Int.*, 2016, **42**(1), p 1640-1647
14. H. Park, J. Kim, S.B. Lee, and C. Lee, Correlation of Fracture Mode Transition of Ceramic Particle with Critical Velocity for Successful Deposition in Vacuum Kinetic Spraying Process, *J. Therm. Spray Technol.*, 2017, **26**(3), p 327-339
15. H.-L. Yao, G.-J. Yang, and C.-J. Li, Molecular Dynamics Simulation and Experimental Verification for Bonding Formation of Solid-State TiO_2 Nano-Particles Induced by High Velocity Collision, *Ceram. Int.*, 2019, **45**(4), p 4700-4706
16. J.-H. Park, D.-S. Park, B.-D. Hahn, J.-J. Choi, J. Ryu, S.-Y. Choi, J. Kim, W.-H. Yoon, and C. Park, Effect of Raw Powder Particle Size on Microstructure and Light Transmittance of α-Alumina Films Deposited by Granule Spray in Vacuum, *Ceram. Int.*, 2016, **42**(2), p 3584-3590
17. J. Exner, M. Hahn, M. Schubert, D. Hanft, P. Fuierer, and R. Moos, Powder Requirements for Aerosol Deposition of Alumina Films, *Adv. Powder Technol.*, 2015, **26**(4), p 1143-1151
18. J. Exner, M. Schubert, D. Hanft, J. Kita, and R. Moos, How to Treat Powders for the Room Temperature Aerosol Deposition Method to Avoid Porous, Low Strength Ceramic Films, *J. Eur. Ceram. Soc.*, 2019, **39**(2–3), p 592-600
19. H. Kwon, H. Park, and C. Lee, Roles of Particle Size Distribution in Bimodal Feedstocks on the Deposition Behavior and Film Properties in Vacuum Kinetic Spraying, *J. Therm. Spray Technol.*, 2018, **27**(5), p 857-869
20. T.-C. Jen, L. Li, W. Cui, Q. Chen, and X. Zhang, Numerical Investigations on Cold Gas Dynamic Spray Process with Nano- and Microsize Particles, *Int. J. Heat Mass Transf.*, 2005, **48**(21–22), p 4384-4396
21. H. Katanoda and K. Matsuo, Gasdynamic Simulation of Aerosol Deposition Method, *Mater. Trans.*, 2006, **47**(7), p 1620-1625
22. W.-Y. Li, H. Liao, H.-T. Wang, C.-J. Li, G. Zhang, and C. Coddet, Optimal Design of a Convergent-Barrel Cold Spray Nozzle by Numerical Method, *Appl. Surf. Sci.*, 2006, **253**(2), p 708-713
23. J. Pattison, S. Celotto, A. Khan, and W. O'neill, Standoff Distance and Bow Shock Phenomena in the Cold Spray Process, *Surf. Coat. Technol.*, 2008, **202**(8), p 1443-1454
24. S.D. Johnson, D. Schwer, D.-S. Park, Y.-S. Park, and E.P. Gorzkowski, Deposition Efficiency of Barium Hexaferrite by Aerosol Deposition, *Surf. Coat. Technol.*, 2017, **332**, p 542-549
25. M. Lee, J. Park, D. Kim, S. Yoon, H. Kim, D. Kim, S. James, S. Chandra, T. Coyle, and J. Ryu, Optimization of Supersonic Nozzle Flow for Titanium Dioxide Thin-Film Coating by Aerosol Deposition, *J. Aerosol Sci.*, 2011, **42**(11), p 771-780
26. K. Naoe, M. Nishiki, and A. Yumoto, Relationship Between Impact Velocity of Al_2O_3 Particles and Deposition Efficiency in Aerosol Deposition Method, *J. Therm. Spray Technol.*, 2013, **22**(8), p 1267-1274
27. H. Park, H. Kwon, and C. Lee, Inflight Particle Behavior in the Vacuum Kinetic Spray Process, *J. Therm. Spray Technol.*, 2017, **26**(7), p 1616-1631
28. D.-M. Chun, J.-O. Choi, C.S. Lee, and S.-H. Ahn, Effect of Stand-Off Distance for Cold Gas Spraying of Fine Ceramic Particles (< 5 μm) Under Low Vacuum and Room Temperature Using Nano-particle Deposition System (NPDS), *Surf. Coat. Technol.*, 2012, **206**(8–9), p 2125-2132
29. A. Fluent, Ansys Fluent Theory Guide, *ANSYS Inc., USA*, 2011, **15317**, p 724-746
30. C. Kleinstreuer and Y. Feng, Computational Analysis of Non-spherical Particle Transport and Deposition in Shear Flow with Application to Lung Aerosol Dynamics—A Review, *J. Biomech. Eng.*, 2013, **135**(2), p 021008
31. H. Park, J. Heo, F. Cao, J. Kwon, K. Kang, G. Bae, and C. Lee, Deposition Behavior and Microstructural Features of Vacuum Kinetic Sprayed Aluminum Nitride, *J. Therm. Spray Technol.*, 2013, **22**(6), p 882-891

32. J. Kwon, H. Park, I. Lee, and C. Lee, Effect of Gas Flow Rate on Deposition Behavior of Fe-Based Amorphous Alloys in Vacuum Kinetic Spray Process, *Surf. Coat. Technol.*, 2014, **259**, p 585-593
33. J. Heo, P. Sudhagar, H. Park, W. Cho, Y.S. Kang, and C. Lee, Room Temperature Synthesis of Highly Compact TiO_2 Coatings by Vacuum Kinetic Spraying to Serve as a Blocking Layer in Polymer Electrolyte-Based Dye-Sensitized Solar Cells, *J. Therm. Spray Technol.*, 2015, **24**(3), p 328-337